Available online at www.sciencedirect.com

SCIENCE DIRECT

Materials Science and Engineering C 25 (2005) 282 – 289

MATERIALS SCIENCE & ENGINEERING C

www.elsevier.com/locate/msec

A novel combinatorial approach to the development of beta titanium alloys for orthopaedic implants

R. Banerjee[a,*], S. Nag[b], H.L. Fraser[b]

[a]Department of Materials Science and Engineering, University of North Texas, Denton, TX, USA
[b]Center for the Accelerated Maturation of Materials, Department of Materials Science and Engineering, The Ohio State University, Columbus, OH, USA

Received 26 November 2004; accepted 5 December 2004
Available online 5 May 2005

Abstract

In recent years there has been a significant thrust directed towards the development of novel implant alloys based on β-Ti. Two recently developed and promising biocompatible β-Ti alloys are Ti–35Nb–7Zr–5Ta and Ti–29Nb–4.6Zr–13Ta. While both these alloy compositions, based on the quaternary Ti–Nb–Zr–Ta system, are promising, there is still a tremendous scope for improvement in terms of alloy design in this and other systems via optimization of alloy composition and thermo-mechanical treatments. Here a novel combinatorial approach has been used for the development of implant alloys with optimized compositions and microstructures. Using directed laser deposition, compositionally graded alloy samples based on the Ti–Nb–Zr–Ta system have been fabricated. These samples have been heat-treated to affect different microstructures in terms of the volume fraction and distribution of the α phase in the β matrix as a function of composition. Subsequently, composition-specific indentation-based hardness and modulus information has been obtained from these samples to construct a database relating the composition and microstructure to the mechanical properties. These databases have been used to train and test fuzzy-logic based neural-network models for predicting the mechanical properties. The trained models have also been used to predict the influence of different alloying additions on the hardness and modulus. These predictions have subsequently been verified by detailed experimental characterization, shedding light on the factors influencing the strength and modulus in these alloys. Such modeling approaches for the development of novel implant alloys can be highly beneficial since they offer the possibility of identifying promising compositions without the necessity for extensive experimental test cycles.

Keywords: Beta titanium alloys; Implants; Biomaterials; Combinatorial; Microstructure-property relationships; Modulus

1. Introduction

The ideal recipe for a biomaterial to be used for implant applications is excellent biocompatibility with no adverse tissue reactions, excellent corrosion resistance in body fluid, high mechanical strength and fatigue resistance, low modulus, low density, and good wear resistance [1,2]. Since the β phase in Ti alloys exhibits a significantly lower modulus than the α phase, and the β alloys also satisfy most of the other requirements for an ideal bioalloy, there is a thrust towards the development of lower modulus β-Ti alloys which retain a single β phase microstructure on rapidly cooling from high temperatures.

Biomedical alloys have widespread application in joint replacement and other orthopaedic surgeries. While the primary properties of interest with respect to biomedical alloys are biocompatibility, corrosion resistance and wear resistance, it is the lack of their load-bearing capability that limits their applicability [1]. For major applications like total joint replacement arthroplasty higher yield strength is essentially coupled with the requirement of a lower modulus approaching that of the human bones [2,3]. Two recently developed promising biomedical alloys, Ti–35Nb–7Zr–5Ta (TNZT) [4] and Ti–12Mo–6Zr–2Fe (TMZF) [5], show significant improvement in these aspects compared to previous generation alloys such as

* Corresponding author. Tel.: +1 940 891 6812; fax: +1 940 565 4824.
E-mail address: banerjee@unt.edu (R. Banerjee).

0928-4931/$ - see front matter © 2005 Elsevier B.V. All rights reserved.
doi:10.1016/j.msec.2004.12.010

Ti–6Al–4V, stainless-steel and cobalt–chromium-based ones. While the mechanical properties and corrosion resistance of Ti–6Al–4V are ideal for implant applications, studies have shown that both V and Al ions may cause long-term health problems. Moreover, the modulus of Ti–6Al–4V (~110 GPa) is substantially higher than that of bone (~10–40 GPa) [2]. Finite-element simulations suggest that joint replacements may better simulate the femur in distributing stress if a lower modulus material is used [6,7]. Large modulus mismatches cause insufficient loading of bone adjacent to the implant (*stress-shielding* phenomena) and eventual failure of the implant [8]. The high modulus of Ti–6Al–4V is attributable to the high volume fraction of the α phase in this alloy. The newer biomedical alloys, such as TNZT and TMZF, exhibit relatively low moduli while maintaining sufficient strength and contain alloying additions that are completely biocompatible. However, the published literature suggests that only a restricted subset of possible alloy compositions in the Ti–Nb–Zr–Ta and Ti–Mo–Zr–Fe complex quaternary systems has been experimentally investigated. In this context it should be recognized that exploration of such quaternary systems over a wide range of compositions is not only experimentally time consuming but also often financially prohibitive. Modeling-assisted combinatorial studies offer a much more attractive alternative.

The titanium-based alloys for biomedical applications usually involve complex multi-component chemistries and often exhibit intricate multi-phase microstructures. The property–microstructure–composition relationships in such alloys are relatively poorly understood. There have been some attempts at understanding the influence of alloying additions to Ti on the modulus and yield strength of these alloys [9,10]. Using a discrete variational cluster method, Song et al. [9] have calculated the equilibrium cluster configurations for various Ti alloys and consequently compared their moduli. In another paper, Kuroda et al. [10] have used a d-electron alloy design approach to model the modulus of various Ti alloys for implant applications. In their approach, the bond order and the metal d-orbital energy level have been mapped on a phase stability diagram for various Ti alloy compositions. Based on their locations on this diagram and their moduli and yield strength, the regions of promising model alloy compositions have been determined [10]. While these approaches are good examples of the use of physics-based modeling for alloy design, they are not always appropriate for complex alloy systems involving a number of different alloying additions. In contrast, rules-based modeling approaches, such as fuzzy-logic models, are particularly useful when handling a large number of composition variables which determine the mechanical properties. In addition, the benefits of fuzzy-logic modeling as compared to other rules-based approaches are that it requires a relatively small database and that the processing steps involved are faster. In the present study, a combinatorial approach, based on laser deposition of compositionally graded alloys, has been used to rapidly develop a database relating composition and microstructure to the mechanical properties. This database, in turn, has been used to train and test fuzzy-logic based neural-network models for predicting the properties and also for determining the relative influence of individual composition and microstructural parameters on the properties.

2. Experimental work

As described above, a novel combinatorial approach has been employed for the rapid assessment of composition–microstructure–property relationships in the Ti–Nb–Zr–Ta alloy system. This combinatorial approach is based on directed laser deposition of compositionally graded alloys using the LENS™ (Laser Engineered Net Shaping) process [11]. A 760 W Nd:YAG laser, which produced near-infrared laser radiation at a wavelength of 1.064 μm, was used for all the depositions. The energy density used was in the range of 30,000 to 100,000 W/cm^2. The oxygen content in the glove box was maintained below 10 ppm during all the depositions. Two types of graded alloys were deposited using a double-powder feeder arrangement, Ti–20Nb–xTa ($0<x<10$) and Ti–xNb–10Zr–5Ta ($20<x<35$) (all in wt.%). In both cases the two hoppers of the powder feeder assembly contained the extrema of the compositions in the graded alloy. For example, in the case of the Ti–xNb–10Zr–5Ta ($20<x<35$) graded alloy, the first hopper contained a blend of elemental powders of composition Ti–20Nb–10Zr–5Ta and the second hopper contained Ti–35Nb–10Zr–5Ta. There was a rectangular parallelepiped geometry of dimension, 1.9 in. (length) × 0.25 in. (width) × 0.52 in. (height) with the compositional grading along the height in steps of 5 wt.% Nb for every 0.13 in. Thus, the deposition was started with only the first powder feeder, containing the Ti–20Nb–10Zr–5Ta powder, operating at 100% of a predetermined optimal flow rate. After a build-up height of ~0.13 in., the flow rate of the first feeder was reduced to 75% while the second feeder containing powder of composition Ti–35Nb–10Zr–5Ta was turned on at a flow rate of 25% of the optimal value. After this second deposit of ~0.13 in., the flow rate of the first feeder was reduced to 50% and that of the second increased to 50% and so on. A similar procedure was used for the Ti–20Nb–xTa deposit with steps of 2 wt.% Ta for every 0.13 in. The as-deposited graded alloy was sectioned along the axis of the parallelepiped and each of the compositions has been subjected to three distinct heat-treatments. The heat-treatments are listed below:

a. solutionizing above the β transus temperature, at 900 °C for 30 min, followed by furnace-cooling,
b. solutionizing above the β transus temperature, at 900 °C for 30 min, followed by air-cooling, and

c. solutionizing above the β transus temperature, at 900 °C for 30 min, followed by air-cooling and ageing at 600 °C for 4 h, followed by air-cooling.

These samples were subsequently mounted for metallographic characterization. The composition and microstructure along the compositional gradient have been characterized in detail using scanning electron microscopy (SEM) and energy dispersive spectroscopy (EDS). The SEM studies have been carried out using a Philips XL30 FEG SEM equipped with an EDAX detector. In addition to the microstructural characterization, the Vickers microhardness and modulus of the graded alloy across the composition gradient have also been measured using a Fischerscope H100C™ microhardness tester. A database has been constructed from these experimental results. This database consists of composition variables (Nb, Zr, and Ta contents), microstructural parameter (volume fraction of α), and the corresponding mechanical properties (microhardness and modulus). The volume fraction of α has been measured using rigorous stereological procedure described elsewhere [12]. The database is shown in Table 1.

In addition, to the SEM studies, TEM studies have also been carried out for some specific compositions and microstructures. Thus, site-specific TEM specimens have been extracted using the Dual-Beam FIB (FEI Strata 235 DB) and subsequently characterized in a Philips/FEI CM200 transmission electron microscope operating at an accelerating voltage of 200 kV.

Table 1
The database generated by the combinatorial approach and used for training and testing the fuzzy-logic models

Ti (wt.%)	Nb (wt.%)	Zr (wt.%)	Ta (wt.%)	VF alpha	*H* (VHN)	*E* (GPa)
66.9	18.0	10.9	4.3	0	473.3	93.25
61.3	23.0	10.6	5.0	0	490.54	122.88
56.2	26.0	10.5	7.3	0	461.22	101.8
61.3	23.0	10.6	5.0	0	470.29	9.42
74.5	19.2	0.0	6.4	0	359.99	107.67
80.3	19.0	0.0	0.6	0	481.69	96.28
76.1	21.4	0.0	2.5	0	435.01	90.43
78.0	16.0	0.0	6.0	0	433.72	89.31
70.5	19.3	0.0	10.2	0	409.58	88.42
68.8	20.1	0.0	11.1	0	383.18	91.27
74.5	18.7	0.0	6.8	52.9	453.62	115.96
69.4	20.4	0.0	10.2	36.2	390.48	119.71
65.4	18.8	10.7	5.2	47.6	423.58	114.86
61.5	22.9	10.2	5.5	35.3	461.43	109.74
76.3	18.2	0.0	5.5	43.6	398.71	120.6
77.3	20.2	0.0	2.5	45.5	462.89	118.41
78.5	21.4	0.0	0.1	41	491.06	123.46
69.1	20.0	0.0	10.9	36.2	420.92	107.19
61.0	24.1	10.7	4.1	36.2	488.73	116.67
66.1	18.2	11.0	4.8	42.9	449.11	105.65
59.6	25.4	10.8	4.3	21	428.92	99.68
53.1	32.1	10.7	4.2	24	466.3	97.34
68.4	19.8	0.0	11.8	55.6	426.27	107.78
70.1	20.1	0.0	9.9	51.2	451.7	110.82
75.3	19.4	0.0	5.3	47.5	403.57	104.22
75.0	21.2	0.0	3.8	45.7	445	113.71
77.9	21.3	0.0	0.9	42.5	443.27	112.76
79.7	19.7	0.0	0.7	39.4	368.1	111.94

3. Fuzzy-logic modeling

Fuzzy logic differs from traditional logic in that a statement can lie on a spectrum from true to false, rather than discretely at either end. Both input and output variables in fuzzy-logic models are associated with adjectives. An adjective specifies a certain range within the overall limits of the variable. This is accomplished by using membership functions associating variables to adjectives. For example, in traditional logic, the adjective "cold" would describe a range of temperatures that is discretely defined, so that, for example, 45° would be cold, and 46° would not. In fuzzy logic, however, a membership function would be used to describe to what extent a temperature is cold, so that while 20° is 100% cold, 45° might only be 50% cold, and then 60° only 20% cold. Membership functions can be plotted on a graph with the value of the variable represented on the abscissa and the degree of membership (varying from 0 to 1) on the ordinate. These membership functions are typically composed of line segments, and often form either an upward-pointing triangle, with the peak at some ideal value for that particular adjective.

Fuzzy variables and adjectives can then be combined in "*if* input variable *is* adjective1 *then* output variable *is* adjective2" rules, where adjective1 is associated with the input variable and adjective2 is associated with the output variable. In addition, the rules for the operators "and," "or," and "not" must be defined to handle degrees of truth—the customary definition is that "and" takes the minimum of the two values, "or" takes the maximum, and "not" returns one minus the degree of truth. Finally, some degree of truth is assigned to a consequent adjective associated with the output variable, and a method for combining multiple consequences must be used to ultimately defuzzify in order to arrive at a value for the output variable. The various methods of combining consequences and defuzzification are beyond the scope of this paper, but further information is available at [13]. The fuzzy-logic models used in the present research effort have been built using the commercially available Cubicalc™ program. This program uses a user-provided database consisting of a number of input and output variables and builds one or more models (depending on the number of output variables). The rules for the fuzzy-logic models are created using a program named Rulemaker which is part of the Cubicalc™ package. Rulemaker employs a neural-network approach for creating the rules [13].

4. Results and discussion

This study focuses on the Ti–Nb–Zr–Ta quaternary alloy system with a special emphasis on understanding the influence of Nb and microstructure on the mechanical properties. Previous research by Ahmed et al. [14] and Niinomi [15] on this alloy system has shown this quaternary alloy system to be one of the most promising for application in orthopaedic implants. As described previously, the database for the fuzzy-logic neural-network model consisted of two output mechanical properties (microhardness in VHN and modulus in GPa) and three compositional variables (Nb, Zr, and Ta contents) as well as one microstructural parameter (volume fraction of α) as inputs. The oxygen content was also measured in some random specimens from alloys of different compositions along the gradient, which had been subjected to the different heat-treatments. No substantial difference was noted in between the oxygen levels in these samples. The average value of oxygen in these samples is ~0.25 wt.%, as measured using chemical analysis. Since no significant differences were observed between different samples in terms of oxygen content, this parameter was not used as an input variable in the database. This database, consisting of 28 datapoints listed in Table 1, was used for training and testing fuzzy-logic neural-network models for predicting the microhardness and the modulus. These models have subsequently been used to predict the values of the mechanical properties for all the 28 datapoints and comparisons of the predicted and experimentally measured microhardness and modulus have been plotted

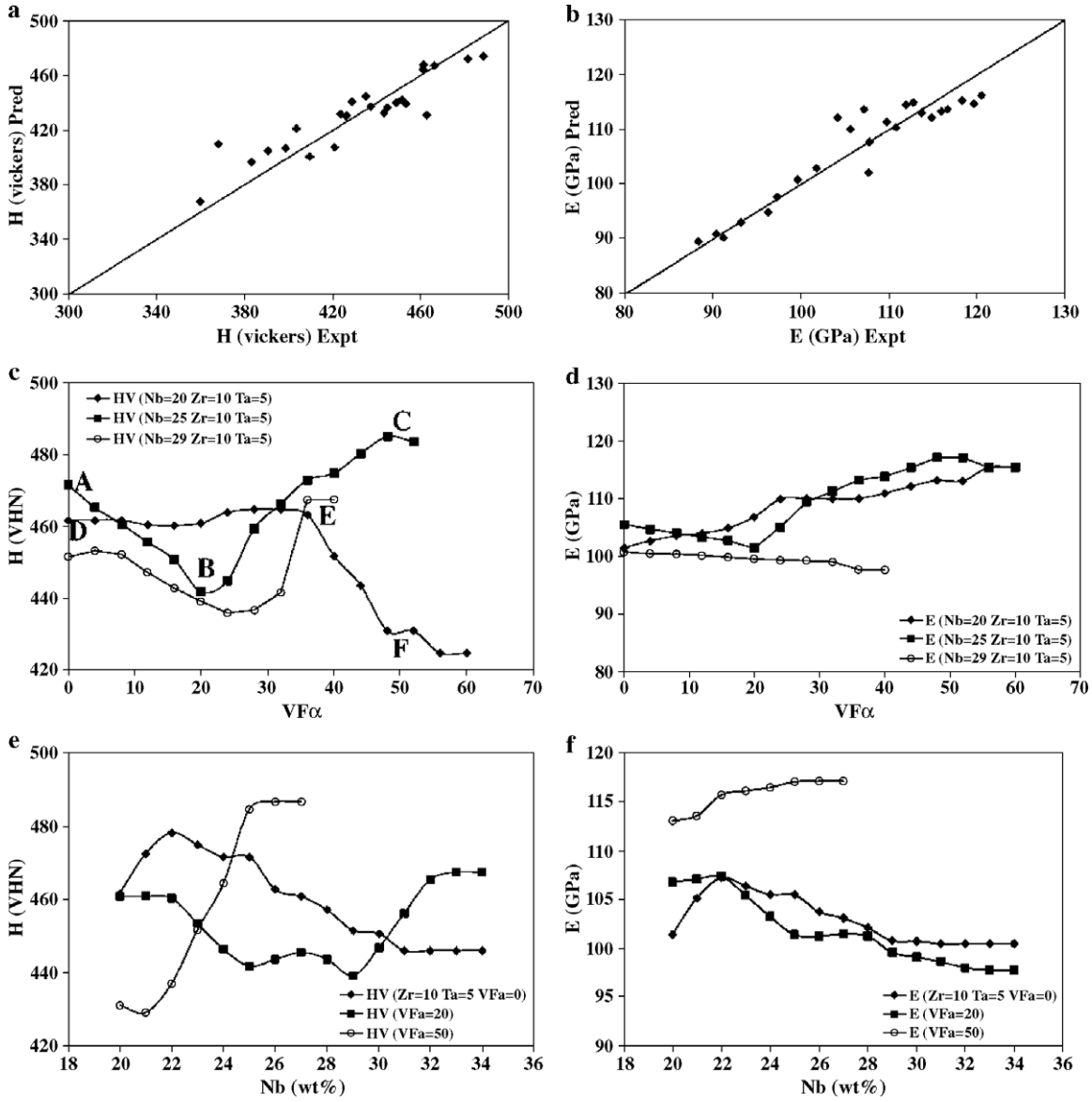

Fig. 1. Plots of the predicted versus experimental values of microhardness (a) and modulus (b) for all the alloys in the database. Plots of the predicted variation of microhardness (c), and modulus (d), with volume fraction of α in a Ti–xNb–10Zr–5Ta alloy for different Nb contents (x=20, 25, 29 wt.% Nb). Plots of the predicted variation of microhardness (e), and modulus (f), with Nb content in a Ti–xNb–10Zr–5Ta alloy for different volume fractions of α (0, 20%, 50% α).

in Fig. 1(a) and (b), respectively. Based on these two plots it appears that the models are reasonably successful in predicting the mechanical properties in this alloy system. However, it should be noted that the predictions afforded by these models are valid only within the composition ranges of the data used for training these models. A powerful way to use these models is to assess the influence of individual input parameters on the mechanical properties. This can be carried out by *virtual* experiments in which all but one of the input parameters are varied. The other input parameters are held constant at specific values thus allowing for an assessment of the sensitivity of one parameter on the properties. Using this methodology, the influence of the volume fraction of α, the microstructural input parameter, on the microhardness and modulus on Ti–Nb–Zr–Ta alloys has been assessed. In Fig. 1(c), the hardness variation has been plotted while in Fig. 1(d), the modulus variation has been plotted for alloys in which the Zr and Ta contents have been maintained at a constant value of 10 wt.% and 5 wt.%, respectively. In each plot, three curves for different Nb contents, 20, 25, and 29 wt.%, are shown. Since these plots are based on *virtual* experiments, the predicted trends can be very useful for assessing qualitative influences of the individual input parameters. In Fig. 1(c), it is rather interesting that for 25 wt.% Nb, as the volume fraction of α increases, there is initially a decrease and eventually an increase in microhardness. The initial decrease in microhardness is unexpected. Furthermore, in the case of 20 wt.% Nb, the microhardness is initially more or less constant with increasing volume fraction of α and decreases beyond ~35 vol.% α as shown in Fig. 1(c). For 29 wt.% Nb the variation in microhardness is similar to that for the 25 wt.% Nb alloy. In the second set of trend plots, the variation in microhardness and modulus has been mapped as a function of Nb content keeping the Zr (= 10 wt.%), Ta (= 5 wt.%), and volume fraction of α constant. Fig. 1(e) shows the variation in hardness while Fig. 1(f) shows the modulus variation as a function of Nb content. In each figure, plots for three different volume fractions of α have been shown, 0%, 20%, and 50%. It is interesting to note that the trend plots are substantially different for the three different volume fractions of α. Thus, for 0% α, the microhardness initially exhibits a small increase following which there is a substantial decrease with increasing Nb content. In the case of 20% α, there is an initial decrease followed by an increase in the microhardness, as shown in Fig. 1(e). Finally, in the case of 50% α, the microhardness shows an increase with increasing Nb content. For the modulus, as shown in Fig. 1(f), while the variations with increasing Nb content are somewhat similar to the microhardness trends, there are some distinct differences which need to be noted. Thus, in the case of 20% α, the modulus continuously decreases with increasing Nb content. In addition, the modulus is substantially higher for all Nb contents in the case of a volume fraction of α equal to 50%, as shown in Fig. 1(f).

In order to develop a critical understanding of the factors leading to these trends in microhardness and modulus in these alloys, detailed TEM studies have been performed in addition to the SEM studies carried out for database development. With reference to the trend plots shown in Fig. 1(c) and (d), specific samples with the same composition, corresponding to the different volume fractions α, have been studied. Thus, for the case of 25 wt.% Nb, three different samples of Ti–25Nb–10Zr–5Ta in air-cooled (equivalent to point A in Fig. 1(c)), aged (equivalent to

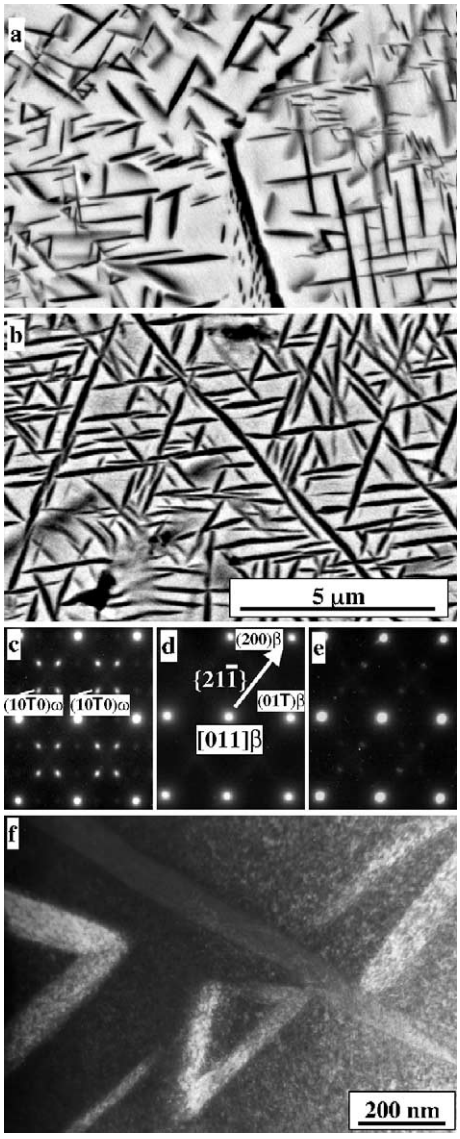

Fig. 2. (a) Backscatter SEM image of the aged Ti–25Nb–10Zr–5Ta alloy. (b) Backscatter SEM image of the furnace-cooled Ti–25Nb–10Zr–5Ta alloy. (c) Selected area diffraction (SAD) pattern along the [011] zone axis of the β phase in the same alloy in the air-cooled condition exhibiting strong reflections from the ω phase. (d) SAD pattern from the same alloy in the aged condition exhibiting negligible ω phase. (e) SAD pattern from the same alloy in the furnace-cooled condition exhibiting negligible ω phase. (f) Bright-field TEM micrograph showing the clustering of α variants in the furnace-cooled alloy of the same composition.

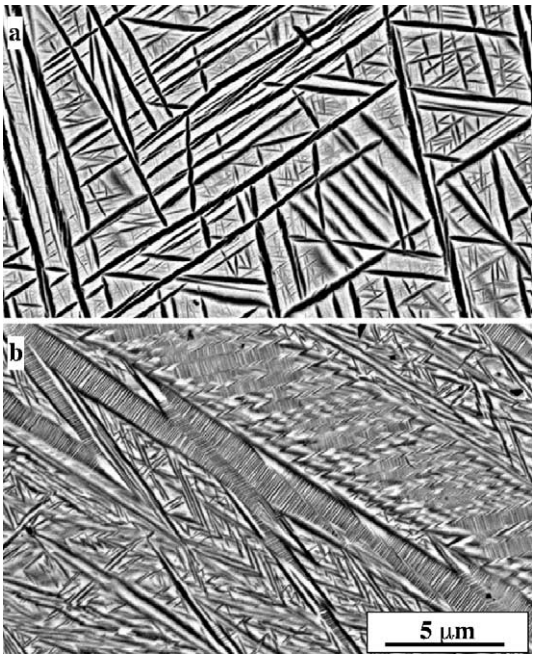

Fig. 3. (a) Backscatter SEM image of the furnace-cooled Ti–20Nb–10Zr–5Ta alloy. (b) Backscatter SEM image of the aged Ti–20Nb–10Zr–5Ta alloy.

point B in Fig. 1(c)), and furnace-cooled (equivalent to point C in Fig. 1(c)) conditions have been chosen. Fig. 2(a) and (b) show backscatter SEM images from the aged and furnace-cooled samples, respectively. The volume fraction of α appears to be higher in the case of the furnace-cooled sample. It should be noted that the air-cooled sample contained 0% α (point A in Fig. 1(c)). Site-specific TEM samples were extracted from these three specimens using the Dual-Beam FIB equipment. Selected area electron diffraction patterns, recorded along the [011] zone axis of the β matrix, from these three samples are shown in Fig. 2(c), (d), and (e). In Fig. 2(c), corresponding to the air-cooled case (point A in Fig. 1(c)), in addition to the fundamental reflections from the β matrix, the diffraction pattern exhibits strong spots at the 1/3 and 2/3 {112} β positions. The presence of these additional reflections is directly indicative of the presence of ω precipitates in this specimen. The strong intensity of these additional reflections suggests a substantial volume fraction of ω in this specimen. In contrast, after ageing, the electron diffraction pattern shown in Fig. 2(d) does not show any additional reflections corresponding to the ω phase. This indicates that the ageing treatment results in the dissolution of ω and the precipitation of secondary α in this specimen leading to an effective decrease in the strength, as reflected in the microhardness trend plot (Fig. 1(c)). In the case of the furnace-cooled specimen, the secondary α laths belonging to different crystallographic variants, and consequently exhibiting different growth directions, tend to cluster in the form of triangle-shaped (2D section view) clusters. This is clearly visible in the SEM micrograph shown in Fig. 2(b) as well as the bright-field TEM micrograph shown in Fig. 2(e).

For the composition Ti–20Nb–10Zr–5Ta, the predicted microhardness trend plot shown in Fig. 1(c) indicates almost no change in hardness with increasing volume fraction of α until ~35%, beyond which there is a rapid decrease in the hardness. In order to investigate the underlying physical reasons, the experimental alloy of composition, Ti–18Nb–10Zr–5Ta in the air-cooled, aged, and furnace-cooled conditions were studied in detail. While this is not exactly the same composition as that shown in the predicted plot (Fig. 1(c)), it is the nearest experimental alloy which was used for training the fuzzy-logic model. Furthermore, predictions for the composition Ti–18Nb–10Zr–5Ta showed the same relative trends as seen in Fig. 1(c). In this case, the air-cooled sample contained 0% α as determined from the SEM studies, and therefore would correspond to point D in Fig. 1(c). The furnace-cooled and aged samples contained ~40% and ~50% α, respectively, and therefore correspond to points E and F in Fig. 1(c), respectively. SEM micrographs from the furnace-cooled and aged samples are shown in Fig. 3(a) and (b), respectively. There is a substantial difference in these two microstructures, not only in terms of the volume fraction, but also the morphology of secondary α. Interestingly, though the aged sample has a higher volume fraction of α, it exhibits a lower microhardness (refer to Fig. 1(c)). In

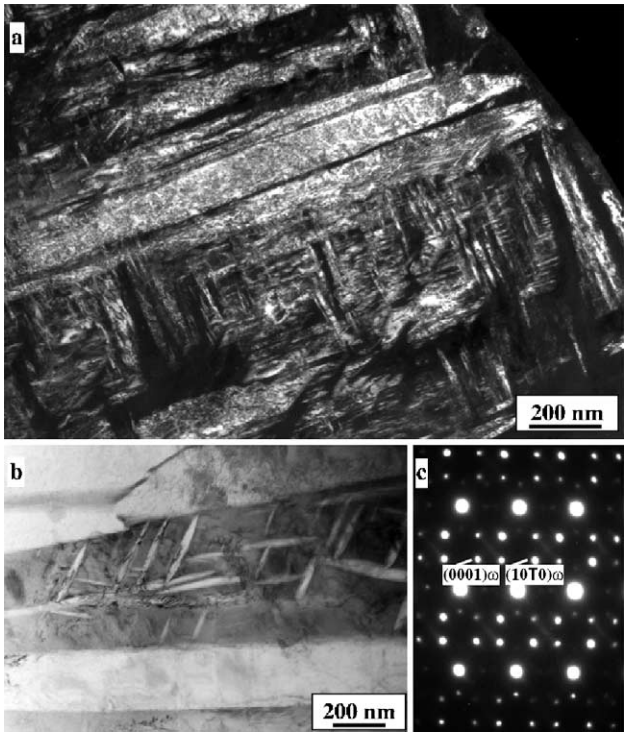

Fig. 4. (a) Dark-field TEM micrograph from the air-cooled Ti–20Nb–10Zr–5Ta alloy showing a large volume fraction of the α″ martensite phase. (b) Bright-field TEM image of the furnace-cooled Ti–20Nb–10Zr–5Ta alloy, exhibiting fine scale tertiary α laths in between secondary α laths. (c) [011] β zone axis SAD pattern from the furnace-cooled Ti–20Nb–10Zr–5Ta alloy, exhibiting strong reflections from the ω phase.

addition, both the air-cooled and furnace-cooled samples exhibit a high microhardness. However, the volume fraction of α is substantially higher in the case of the furnace-cooled sample. In order to rationalize these observations, TEM studies have been conducted on all three of these samples and site-specific specimens have been prepared using the Dual-Beam FIB. Fig. 4(a) shows a dark-field TEM micrograph from the air-cooled sample, exhibiting a very high volume fraction of the martensitic α″ phase in the microstructure. Thus, the lack of any contrast in the backscatter SEM images from the same sample can be explained due to the compositional invariance between the matrix and the martensitic phase. However, the high volume fraction of martensite is the reason for the high microhardness exhibited by this sample. Furthermore, on ageing the martensite, it decomposes to the α+β structure shown in Fig. 3(b), corresponding to a lower microhardness. A bright-field TEM image of the furnace-cooled sample is shown in Fig. 4(b). In addition to the coarser secondary α laths, some fine scale tertiary α laths are visible in this micrograph. A selected area diffraction pattern from only the β matrix in this sample, recorded along the [011] β zone axis, is shown in Fig. 4(c). The presence of strong additional reflections at the 1/3 and 2/3 {112} β locations indicates a substantial volume fraction of ω in this sample. The coupled effect of the ω and the fine scale tertiary α is likely to lead to a high microhardness in the furnace-cooled sample as predicted in the trend plot shown in Fig. 1(c). In summary, the change in volume fraction of α can have different types of influences on the strength (as measured by microhardness) in these alloys for different compositions. Furthermore, the thermal treatment leading to the specific microstructure also influences the microhardness. For a lower Nb content, while there is no α formation in the faster air-cooled condition, the α″ martensite formation results in a high hardness. While furnace-cooling does not lead to α″ formation, the combination of fine scale α together with ω in the retained β matrix still results in a high hardness. However, while ageing the martensite leads to a high volume fraction of α, the softer nature of the α phase as compared to the α″ martensite couple with the lack of ω in the aged sample results in a decrease in the microhardness.

Consider the predicted trend plots in Fig. 1(e) and (f) showing the variation of microhardness and modulus as a function of Nb content in these alloys for three different volume fractions of α. Based on the experimental results discussed previously, it appears that the overall decrease in microhardness, with increasing Nb content, in the Ti–*x*Nb–10Zr–5Ta system for 0% α is a result of the dissolution of the ω phase. The ω phase de-stabilizes with increasing Nb content in the β phase. However, it should be noted that for 0% α and low Nb contents, the martensitic α″ phase could be present in the microstructure, as discussed previously. Therefore, the initial increase in the microhardness for the 0% α curve (Fig. 1(e)) can be attributed to a combined effect of both α″ and ω phases in the microstructure. For 20% α, the microhardness initially decreases and subsequently increases beyond ~29 wt.% Nb (refer to Fig. 1(e)). While the initial decrease in hardness can be attributed to the dissolution of ω, the subsequent increase cannot be attributed to α since the volume fraction of α is held constant at 20% for this trend plot. Therefore, it is likely that the increase in hardness is a result of solid solution strengthening of the β matrix in these alloys which becomes a dominant strengthening mechanism beyond a certain Nb content in these alloys. Interestingly, the corresponding trend plots for the modulus, shown in Fig. 1(f), exhibit a different nature. Thus, while the trend in modulus with increasing Nb content is similar to that of the microhardness in the case of the 0% α curve, the modulus variations differ quite substantially from the microhardness variations in the case of the 20% α curve. Thus, the modulus keeps constantly decreasing with increasing Nb content in this case. The initial decrease in this case too can be attributed to dissolution of ω, similar to the case of the microhardness observations. However, the continued decrease in modulus for richer Nb contents suggests that the additional Nb in the β matrix is actually leading to a reduction in the modulus of the β phase. The assumption here is that the Nb primarily segregates to the β phase. Previous published results on binary Ti–Mo alloys indicate that with increasing Mo addition, the modulus of the β phase initially decreases quite substantially and subsequently increases [16]. Therefore, it is likely that Nb additions have similar effects on the modulus of β-Ti. Thus, the present experimental results indicate that for the 20% α case, the composition of the β phase is within the regime of decreasing modulus for the range of Nb contents considered. However, when the volume fraction of α is 50%, the remaining β phase is likely to be highly enriched in Nb and could possibly lead to an increased modulus of β, as shown in Fig. 1(f). In any case, for such a high volume fraction of α, the modulus is expected to be quite high since in general the α phase exhibits a much higher modulus as compared with the β phase. For the same 50% α case, the microhardness variations (shown in Fig. 1(e)) indicate a steep rise with Nb content. As discussed previously for the 20% α case, one of the possible reasons for this rise can be attributed to the solid solution strengthening due to increasing Nb in the β matrix. However, it should be noted that the low microhardness for the 50% α curve, near the Ti–20Nb–10Zr–5Ta composition, could also be the result of a softer α phase arising from the decomposition of the α″ martensitic phase on ageing. Comparing the three trend plots in Fig. 1(e), it can be concluded that the ω phase is likely to have a more pronounced effect on the microhardness as compared to the secondary α precipitates. In contrast, the α phase has a much more pronounced effect on the modulus as compared with the ω phase, as shown in Fig. 1(f).

One of the interesting features of this study is that it leads to certain insights regarding the optimal microstructural conditions required for balancing the strength (as

measured by microhardness) and the modulus. For example, referring to Fig. 1(e) and (f), it appears that for a composition of Ti–32Nb–10Zr–5Ta, having 20% α in the microstructure could be quite beneficial since it enhances the strength while still maintaining a relatively low modulus. In contrast, in the absence of any α in the microstructure, the same composition would result in substantially lower strength and a similar modulus. This example illustrates the importance of microstructural engineering in developing the optimum balance of the mechanical properties of interest in these alloys.

5. Summary

A novel combinatorial approach for rapid assessment of the mechanical properties for a range of compositions of promising Ti alloys for implant applications has been discussed in this paper. This approach is based on the use of laser-deposited compositionally graded alloys. The microhardness and modulus of these alloys have been measured using indentation-based techniques. These experimental results have been used to rapidly populate a database which, in turn, has been used to train and test rules-based fuzzy-logic models for predicting mechanical properties. The predictions afforded by these models have been used to investigate the sensitivity of the mechanical properties on the individual input parameters, i.e. composition and/or microstructure. The predicted trend plots suggest possible strengthening mechanisms and factors influencing the modulus in these alloys. For certain cases, these factors have been validated by detailed TEM and SEM studies of the microstructure. Thus, by employing such a combination of experimental and modeling techniques via a combinatorial approach, it is possible to accelerate the maturation of existing implant alloys and the development of new ones.

References

[1] K. Wang, The use of titanium for medical applications in the USA, Mater. Sci. Eng., A Struct. Mater.: Prop. Microstruct. Process. 213 (1996) 134–137.
[2] M.J. Long, H.J. Rack, Titanium alloys in total joint replacement—a materials science perspective, Biomaterial 19 (1998) 1621–1639.
[3] E.W. Lowman, Osteoarthiritis, J. Am. Med. Acad. 157 (1955) 487.
[4] T.A. Ahmed, M. Long, J. Silverstri, C. Ruiz, H.J. Rack, A new low modulus biocompatible titanium alloy, Titanium 95': Sci. Technol. (1996) 1760–1767.
[5] K. Wang, L. Gustavson, J. Dumbleton, The characterization of Ti–12Mo–6Zr–2Fe. A new biocompatible titanium alloy developed for surgical implants, Beta Titanium in the 1990's, The Mineral Metals and Materials Society, Warrendale, Pennsylvania, 1993, pp. 2697–2704.
[6] E. Cheal, M. Spector, W. Hayes, Role of loads and prosthesis material properties on the mechanics of the proximal femur after total hip arthoplasty, J. Orthoptera. Res. 10 (1992) 405–422.
[7] P. Prendergast, D. Taylor, Stress analysis of the proximo-medial femur after total hip replacement, J. Biomed. Eng. 12 (5) (1990) 379–382.
[8] W.F. Ho, C.P. Ju, J.H. Chern Lin, Structure and properties of cast binary Ti–Mo alloys, Biomaterial 20 (1999) 2115–2122.
[9] Y. Song, D.S. Xu, R. Yang, D. Li, W.T. Wu, Z.X. Guo, Theoretical study of the effects of alloying elements on the strength and modulus of β-type bio-titanium alloys, Mater. Sci. Eng., A Struct. Mater.: Prop. Microstruct. Process. 260 (1999) 269–274.
[10] D. Kuroda, M. Niinomi, M. Morinaga, Y. Kato, T. Yashiro, Design and mechanical properties of new β type titanium alloys for implant materials, Mater. Sci. Eng., A Struct. Mater.: Prop. Microstruct. Process. 243 (1998) 244–249.
[11] D.M. Keicher, J.E. Smugeresky, JOM 49 (5) (1997) 51–54.
[12] J. Tiley, T. Searles, E. Lee, S. Kar, R. Banerjee, J.C. Russ, H.L. Fraser, Quantification of microstructural features in α/β titanium alloys, Mater. Sci. Eng., A Struct. Mater.: Prop. Microstruct. Process. 372 (1–2) (2004) 191.
[13] http://www.hyperlogic.com.
[14] T. Ahmed, M. Long, J. Silvestri, C. Ruiz, H.J. Rack, A new low modulus, biocompatible titanium alloy, Titanium'95: Sci. Technol. (1995) 1760–1767.
[15] M. Niinomi, Fatigue performance and cyto-toxicity of low rigidity titanium alloy, Ti–29Nb–13Ta–4.6Zr, Biomaterial 24 (2003) 2673–2683.
[16] W.F. Ho, C.P. Ju, J.H. Chern Lin, Structure and properties of cast binary Ti–Mo alloys, Biomaterial 20 (1999) 2115.